Monthly Notices
of the
ROYAL ASTRONOMICAL SOCIETY

MNRAS **528,** 757–770 (2024) https://doi.org/10.1093/mnras/stad3910
Advance Access publication 2023 December 21

Tidally offset neutral gas in Lyman continuum emitting galaxy Haro 11

Alexandra Le Reste,[1★] John M. Cannon,[2] Matthew J. Hayes,[1] John L. Inoue,[2] Amanda A. Kepley,[3] Jens Melinder,[1] Veronica Menacho,[1] Angela Adamo,[1] Arjan Bik,[1] Timmy Ejdetjärn,[1] Gyula I. G. Józsa,[4,5] Göran Östlin[1] and Sarah H. Taft[2,6]

[1]*The Oskar Klein Centre, Department of Astronomy, Stockholm University, AlbaNova, SE-10691 Stockholm, Sweden*
[2]*Department of Physics and Astronomy, Macalester College, 1600 Grand Avenue, Saint Paul, MN 55105, USA*
[3]*National Radio Astronomy Observatory, 520 Edgemont Road, Charlottesville, VA 22903-2475, USA*
[4]*Max-Planck-Institut für Radioastronomie, Auf dem Hügel 69, D-53121 Bonn, Germany*
[5]*Department of Physics and Electronics, Rhodes University, PO Box 94, Makhanda, 6140, South Africa*
[6]*Minnesota Institute for Astrophysics, School of Physics & Astronomy, University of Minnesota, 116 Church St. SE, Minneapolis, MN 55455, USA*

Accepted 2023 December 14. Received 2023 December 1; in original form 2023 July 14

ABSTRACT

Around 400 Myr after the big bang, the ultraviolet emission from star-forming galaxies reionized the Universe. Ionizing radiation (Lyman continuum, LyC) is absorbed by cold neutral hydrogen gas (H I) within galaxies, hindering the escape of LyC photons. Since the H I reservoir of LyC emitters has never been mapped, major uncertainties remain on how LyC photons escape galaxies and ionize the intergalactic medium. We have directly imaged the neutral gas in the nearby reionization-era analogue galaxy Haro 11 with the 21 cm line to identify the mechanism enabling ionizing radiation escape. We find that merger-driven interactions have caused a bulk offset of the neutral gas by about 6 kpc from the centre of the galaxy, where LyC emission production sites are located. This could facilitate the escape of ionizing radiation into our line of sight. Galaxy interactions can cause both elevated LyC production and large-scale displacement of H I from the regions where these photons are produced. They could contribute to the anisotropic escape of LyC radiation from galaxies and the reionization of the Universe. We argue for a systematic assessment of the effect of environment on LyC production and escape.

Key words: ISM: lines and bands – galaxies: interactions – galaxies: ISM – galaxies: starburst – radio lines: galaxies – ultraviolet: galaxies.

1 INTRODUCTION

The Universe underwent a major phase change during which almost all intergalactic hydrogen was ionized about 13 billion years ago: cosmic reionization (Barkana 2006). Reionization is thought to have been driven by strong ultraviolet (UV) emission from massive stars within primeval star-forming galaxies (Robertson et al. 2010; Kulkarni, Worseck & Hennawi 2019; Dayal et al. 2020; Trebitsch et al. 2023). Lyman continuum (LyC) emission is absorbed by cold neutral hydrogen gas in the interstellar medium of galaxies, hindering the escape of ionizing radiation to the intergalactic medium. Observations of galaxies at this epoch lack spatial resolution, thus nearby analogues of early galaxies have been used to understand the detailed physical processes responsible for reionization (Izotov et al. 2016; Senchyna et al. 2017; Izotov et al. 2018; Berg et al. 2019; Flury et al. 2022a). UV absorption-line measurements suggest that the main property driving LyC escape is a low covering fraction of the neutral gas (Gazagnes et al. 2018; Saldana-Lopez et al. 2022), with LyC photons escaping through ionized channels within the interstellar medium. However, absorption measurements do not characterize the interstellar medium in the full physical volume covered by dense neutral gas in galaxies.

The 21 cm line of hydrogen is the only direct tracer of H I gas that can probe the entire extent of the material inhibiting LyC escape. H I has never been mapped in confirmed LyC emitters, leaving major uncertainties on how LyC photons escape galaxies and ionize the intergalactic medium (MacHattie et al. 2014; Pardy et al. 2016; Puschnig et al. 2017; Taft et al. 2019). Furthermore, even with upcoming state-of-the-art facilities, it will be impossible to observe resolved H I in emission in galaxies at the Epoch of Reionization (Ghara et al. 2017). Thus, observing H I in nearby galaxies with detected ionizing LyC emission is necessary for a complete understanding of the gas removal and ionization mechanisms at play during the Epoch of Reionization.

Haro 11 is the closest (D = 93 Mpc) confirmed LyC-emitting galaxy (Bergvall et al. 2000), and one of the only three known LyC-leaking galaxies that are sufficiently close to be observed and resolved in 21 cm (Bergvall et al. 2006; Leitet et al. 2013; Leitherer et al. 2016). The UV photons in this star-forming galaxy are produced in three distinct regions (Kunth et al. 2003; Adamo et al. 2010; Sirressi et al. 2022) labelled Knots A, B, and C, shown in Fig. 1 (panel B), with Knot B having the largest photoionization rate of all three regions (Sirressi et al. 2022). The global neutral gas distribution that can allow for the anisotropic escape of ionizing

---

[★] E-mail: alereste@umn.edu

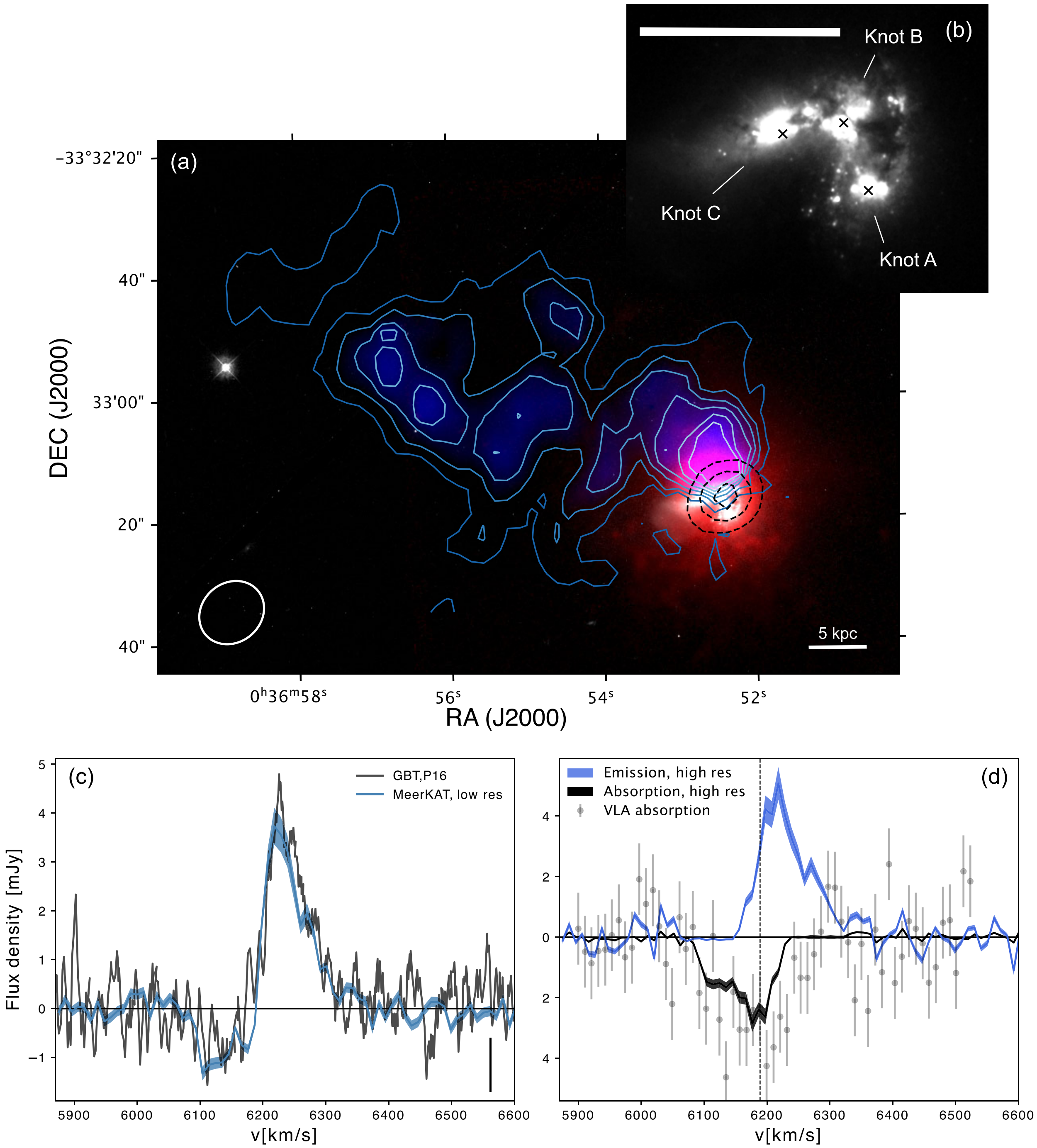

Figure 1. Neutral gas in Haro 11. Panel A: Colour-composite image of Haro 11 with 21 cm contours. High resolution (10 arcsec) MeerKAT 21 cm emission is shown in blue with solid blue contours overlaid, MUSE H α emission is shown in red and *HST* optical stellar light observed using the *F435W* filter in white. The MeerKAT emission contours are shown with levels $N_{\mathrm{H\,I}} = \{0.7, 1.4, 2.1, 2.8, 3.4, 4.1\} \times 10^{20}\,\mathrm{cm}^{-2}$ (0.007–0.04 Jy beam^{-1} km s^{-1}), corresponding to the 5σ to 30σ levels, with lower σ contours shown in darker shades of blue. MeerKAT 21 cm absorption contours are overlaid in dashed black lines, with levels $\{-0.3, -0.2, -0.1\}$ Jy beam^{-1} km s^{-1} displayed. The MeerKAT synthesized beam is shown by a white ellipse in the lower left corner of the image. Panel B: Stellar light shown by the *HST F435W* image, with star-forming knots identified by crosses. In panel A and B, a white bar indicates the scale corresponding to 5 kpc. In all images, North is up and East is to the left. Panel C: Low angular resolution (47 arcsec) MeerKAT 21 cm spectrum integrated over all detected 21 cm (emission and absorption), shown in blue. The GBT spectrum is shown in grey for comparison. A vertical black bar on the bottom right corner shows the typical error on the GBT spectrum. Panel D: MeerKAT 21 cm high angular resolution (10 arcsec) emission (blue) and absorption (black) spectra, integrated over the regions shown respectively by blue and black contours in panel A. The VLA absorption spectrum is shown with grey dots for comparison. The vertical dashed line shows the velocity centroid of ionized gas around the star-forming knots, where the sources emitting the absorbed radio continuum radiation are located.

Table 1. Very Large Array radio continuum observation parameters.

Band	*S* band	*X* band	*Ka* band
Configuration	B	CnB	DnC
Central frequency (GHz)	3	9.8	33.0
Bandwidth (GHz)	1.75	4.0	7.9
Channel width (MHz)	1	1	1
Number of channels	128	128	128
Number of spectral windows	16	32	64
Flux/BP calibrator	3C48	3C48	3C48
Phase calibrator	J0024-4202-S	J0012-3954	J0012-3954
Phase calibrator cadence (min)	14	14	7
Time on source (h)	0.26	0.24	3.1
Observing dates	2016-05-31	2016-05-05	2016-01-10 to 2016-01-24
Beam	5.3 arcsec × 1.65 arcsec	3.22 arcsec × 1.51 arcsec	2.31 arcsec × 1.35 arcsec
Image noise (mJy beam^{-1})	15.6	9.1	6.7

radiation out of the galaxy has not been measured. The molecular gas distribution has been measured (Gao et al. 2022), but molecular gas is a negligible source of LyC opacity in galaxies as compared to neutral gas. Previous single dish observations of Haro 11 detected the 21 cm in emission (Pardy et al. 2016). However, the distribution of the gas has remained unknown due to insufficient sensitivity of interferometric observations, with only unresolved 21 cm absorption detections (MacHattie et al. 2014; Taft et al. 2019). In this paper, we present observations of the galaxy in 21 cm obtained with the MeerKAT telescope that provides increased surface brightness sensitivity as compared to interferometers previously available for H I observations. In Section 2, we present the observations, in Section 3 we characterize the radio continuum source in Haro 11, in Section 4 and 5 we detail the neutral gas content and geometry of the system respectively, we discuss our findings in Section 6, and present our concluding remarks in Section 7.

Throughout this paper, we assume a Hubble constant $H_0 = 67.4 \pm 0.5\,\mathrm{km\,s^{-1}\,Mpc^{-1}}$ and a matter density $\Omega_\mathrm{m} = 0.315$ (Planck Collaboration VI 2020). Using the redshift of Haro 11 ($z = 0.0206$; Bergvall et al. 2000), we derive a luminosity distance of 93 Mpc. Literature values mentioned here have been corrected for this value.

2 OBSERVATIONS AND DATA REDUCTION

2.1 MeerKAT 21 cm observations

Haro 11 was observed with the MeerKAT interferometer as part of programme SCI-20210212-AL-01 (PI: Le Reste). The 8.8 h of on-source integration time were split between two observing sessions (2021 February 20 and 2021 August 14). The correlator was configured in the C856M32k mode, wherein an 856 MHz wide bandpass is separated into 32 768 channels. J0408-6545 and J1939-6342 were used for primary flux and bandpass calibrations for the February 20 and the August 14 data, respectively; J0025-2602 was used as secondary calibrator in both observing sessions. To study the 21 cm H I line, a narrow (20 MHz) bandpass, centred on the recessional velocity of Haro 11 derived from optical emission lines (Bergvall et al. 2000), was extracted from the full data set. The 26.123 kHz channel width produces a native velocity resolution of 5.5 km s^{-1}. Data reduction and calibration followed standard prescriptions in the CASA 5.6 environment (CASA Team 2022). The calibrated data set was continuum-subtracted using the task `uvcontsub`. Imaging was performed with CASA 6.4 using the `AUTO-MULTITHRESH` algorithm (Kepley et al. 2020) within the `tclean` task. Three clean data cubes with different angular resolutions were produced by using tapering in the uv-plane, each with velocity resolution set to 10 km s^{-1}. The masks generated by `AUTO-MULTITHRESH` were visually examined, and deep cleaning (to 0.5 σ) was performed inside regions containing 21 cm signal. Visual examination confirmed the presence of 21 cm absorption in the cube, which had been detected by high angular resolution interferometric observations previously (MacHattie et al. 2014). The final datacubes have beam sizes and rms noise values as follows: 47.3 arcsec × 45.7 arcsec and $\sigma = 0.18$ mJy beam^{-1} (‘low resolution’, produced using a 2.5kλ uv-taper); 24.6 arcsec × 21.7 arcsec and $\sigma = 0.16$ mJy beam^{-1} (‘medium resolution’, produced using a 7k uv-taper); 11.2 arcsec × 9.7 arcsec and $\sigma = 0.17$ mJy beam^{-1} (‘high resolution’, produced with no uv-taper).

The dedicated 21 cm detection software Source FInding Algorithm (SOFIA, version 1.3.3; Serra et al. 2015) was used to detect 21 cm signal in the cubes. The Smooth + Clip algorithm was used with 4.5σ threshold and median absolute deviation rms mode in order to include H I absorption in the mask. Spatial smoothing with Gaussian kernels and spectral smoothing boxcar kernels (either no smoothing or $\sim$ 30 km s^{-1} smoothing) were used. For each of the datasets, kernels with no smoothing, 10 arcsec smoothing, 23 arcsec smoothing, and 46 arcsec smoothing were applied. Eye inspection of the masked cubes confirmed that the 21 cm detection parameters enabled the recovery of all H I emission and absorption in the cubes.

2.2 VLA radio continuum data

In order to characterize the strong radio continuum source against which 21 cm absorption occurs, we used archival radio continuum data. The data were taken by the National Radio Astronomy Observatory’s Karl G. Jansky Very Large Array (VLA) as part of project VLA/15B-197 (PI: Kepley). As part of the project, Haro 11 was observed with the *S*, *X*, and *Ka* bands. The observing frequencies and parameters are given in Table 1. For all three bands observed, a flux/bandpass calibrator was observed once during each scheduling block and the phase calibrator was observed periodically. Additionally for the *X*- and *Ka*-band data, a pointing scan was run at the beginning of a scheduling block. The data were calibrated using VLA pipeline version Pipeline-Cycle3-R1-B with CASA version 4.3.1 r32491 and imaged in CASA 6.2.1–7, using multiterm, multifrequency synthesis (Rau & Cornwell 2011) with nterms = 2 to account for the spectral curvature of the data and Briggs robust weighting of 0.5. In addition, the *S*-band data used w-projection to correct for

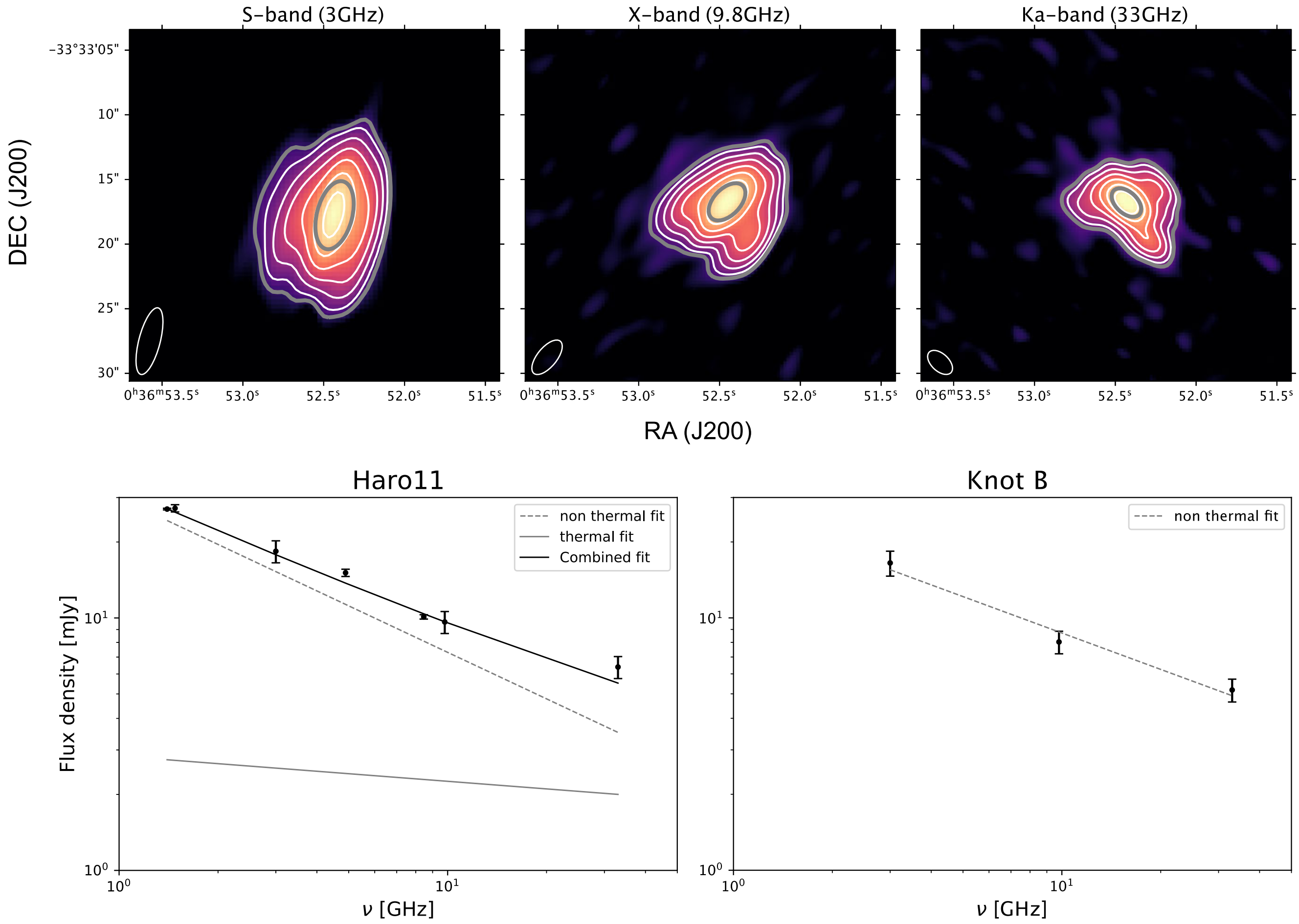

Figure 2. Radio continuum in Haro 11. The panels on the top row show, from left to right, the *S*-band (3 GHz), *X*-band (9.8 GHz), and *Ka*-band (33 GHz) continuum images. Intensities are displayed with a logarithmic stretch to highlight the full distribution of the radio continuum emission. The white contours displayed correspond to the 5σ, 10σ, 20σ, 40σ, 80σ, and 160σ levels. The synthesized beam is represented by a white ellipse in the bottom left corner. The contours used to extract the radio continuum flux from Haro 11 (3σ level) and Knot B (Gaussian fit) are shown in grey. The bottom row panels show the SED for Haro 11 (left) and star-forming Knot B only (right). For Haro 11, we fit the data using a combination of thermal and non-thermal radiation. The combined fit is shown in black, the thermal and non-thermal components are shown in grey solid and dashed lines, respectively. For Knot B, we fit the data using the non-thermal emission only (grey dashed line), since we do not have enough data points to make a combined fit.

the curvature of the sky over the larger field of view. We used self-calibration to improve the image dynamic range for all three bands. All three data sets had a phase self-cal performed. The *Ka*-band data had an additional scan-length amplitude self-cal. The final images were primary beam corrected accounting for the variation of the primary beam as a function of frequency across the band.

3 RADIO CONTINUUM EMISSION

We present the VLA radio continuum images of Haro 11 in the top panels of Fig. 2. The radio continuum flux density of Haro 11 was calculated in the VLA archival images using the lowest contour shown in Fig. 2, corresponding to the 3σ noise level. The flux density in all three bands observed with the VLA was supplemented by values taken from the literature (Schmitt et al. 2006; MacHattie et al. 2014). The flux density values for Haro 11 are presented in Table 2.

While radio continuum emission is produced across the optical body of the galaxy, the strongest source is co-spatial with star-forming Knot B, and is unresolved, even with *Ka*-band imaging. In fact, the radio continuum emission in Haro 11 is completely dominated by the contribution from Knot B. We compare the radio continuum morphology and the location of the Knot B radio continuum emission with the optical image of Haro 11 in Appendix Fig. A1. X-ray observations of the galaxy found two ultraluminous X-ray regions, respectively, overlapping with Knots C and B (Prestwich et al. 2015; Gross, Prestwich & Kaaret 2021). These observations could indicate the presence of a low-luminosity active galactic nucleus (AGN) in the X-ray region co-spatial with Knot B. We extract the flux density in Knot B only in the VLA archival images. To do so, we fit a 2D Gaussian using the CASA task `imfit`, fixing the value of the peak and allowing for a zero-point offset. The flux density values of Knot B only are presented in Table 2. The error values are calculated using a conservative flux calibrator error of 10 per cent, which drives the uncertainty.

We show the flux extraction regions used for the full galaxy and Knot B in Fig. 2. We fit the radio spectral energy distribution (SED) of Haro 11 using a combination of thermal and non-thermal radiation: $S(\nu) = S_{nth} + S_{th} = c_1\,\nu^{-\alpha} + c_2\nu^{-0.1}$. We use a least-squares fitting approach weighted by errors and find the following parameters produce the best fit to the data: $c_1 = 29.9 \pm 4.5$ mJy,

Table 2. Radio continuum flux density values for Haro 11 and Knot B only.

ν (GHz)	1.4	1.48	3	4.89	8.46	9.8	33
$S_{\nu,\mathrm{Haro11}}$ (mJy)	27.0 ± 0.2	$27.20.9 \pm 0.9$	18.4 ± 1.8	15.1 ± 0.5	10.1 ± 0.2	9.6 ± 1.0	6.4 ± 0.6
$S_{\nu,\mathrm{KnotB}}$ (mJy)	–	–	16.5 ± 1.7	–	–	8.0 ± 0.8	5.1 ± 0.5

Table 3. Neutral gas properties of Haro 11 and different components in the galaxy.

$S_{\mathrm{H\,I,em}}$	$0.391 \pm 0.042\,\mathrm{Jy\,km\,s^{-1}}$
$M_{\mathrm{H\,I,em}}$	$7.99 \pm 0.85 \times 10^8\,\mathrm{M_\odot}$
$M_{\mathrm{H\,I,abs}}$	$3.10 \pm 1.16 \times 10^8\,\mathrm{M_\odot}$
$M_{\mathrm{H\,I,tot}}$	$1.11 \pm 0.20 \times 10^9\,\mathrm{M_\odot}$
$M_{\mathrm{H\,I,tail}}$	$6.72 \pm 0.88 \times 10^8\,\mathrm{M_\odot}$

$\alpha = 0.6 \pm 0.27$, $c_2 = 2.8 \pm 5.3$ mJy. Given the errors on the thermal emission coefficient, the radio continuum emission in Haro 11 is consistent mostly with non-thermal emission, and is dominated by the emission from Knot B. The non-thermal spectral slope is consistent with radio emission from star-forming regions (Klein, Lisenfeld & Verley 2018). We fit the SED of Knot B with non-thermal radiation only, given the number of points is insufficient for a combined fit, and will lead to overfitting. We find the following parameters minimize the chi-square: $c_1 = 26.3 \pm 5.1$ mJy, $\alpha = 0.5 \pm 0.1$. The flatter spectral index of Knot B is consistent within errors with that of the galaxy, and is consistent with that of star-forming regions. Therefore, we cannot conclude on the presence or absence of an AGN with the radio continuum observations.

4 THE NEUTRAL GAS CONTENT OF HARO 11

The MeerKAT 21 cm H I image and spectra are presented in Fig. 1 with the Hα emission of Haro 11 from MUSE (Menacho et al. 2019) tracing ionized gas and optical stellar light from *HST* filter *F*435*W* imaging (Östlin et al. 2009). We detect and resolve H I in emission that was previously detected (Fig. 1, panel C) by the Green Bank Telescope (GBT) (Pardy et al. 2016) and detect the unresolved absorption component (Fig. 1, panel D) detected by the VLA (MacHattie et al. 2014; Taft et al. 2019).

4.1 H I mass estimation

The MeerKAT 21cm high angular resolution cube was used for most of the H I science applications, as the resolution allows to separate the 21 cm emission and the significant 21 cm absorption components. We have summarized the H I properties of the galaxy in Table 3, and detail the methods used to obtain these values below. To estimate the gas mass associated with 21 cm emission only, the absorption component was manually masked from the cube. A double Gaussian function was fitted to the emission profile using least-squares fitting weighted by errors. The fitted profile was integrated, yielding the 21 cm emission flux $S_{\mathrm{H\,I,em}} = 0.391 \pm 0.042\,\mathrm{Jy\,km\,s^{-1}}$. Flux error estimation accounts for a conservative flux calibrator error of 10 per cent, the variance in the cube and the uncertainty on fitting parameters. To determine the emitting gas mass, we assume that the gas is optically thin and use the standard equation (e.g. Roberts 1962)

$$M_{\mathrm{H\,I}}\,(\mathrm{M_\odot}) = 2.36 \times 10^5 D^2\,(\mathrm{Mpc})\, S_{\mathrm{H\,I}}\,(\mathrm{Jy\,km\,s^{-1}}). \qquad (1)$$

This yields a new mass estimate for the H I in emission $M_{\mathrm{H\,I,em}} = 7.99 \pm 0.85 \times 10^8\,\mathrm{M_\odot}$, a value larger than that of $5.7 \pm 0.8 \times 10^8\,\mathrm{M_\odot}$ previously calculated with the single-dish measurement (Pardy et al. 2016). Values differ owing to the possibility to differentiate between the emission and absorption components with the MeerKAT observation, which average each other out in the unresolved GBT observation.

The gas mass associated with 21 cm absorption was estimated separately, by inverting the absorption component mask to mask all emission. The calculation requires an assumption on the volume covered by the gas, and is a function of the area covered by the gas A_{gas}, the column density $N_{\mathrm{H\,I}}$, the mass of the hydrogen atom m_{H} and the volume filling factor, which is a function of the gas covering fraction f. We assume the same volume filling factor $f^{3/2}$ as in the previous 21 cm absorption study of Haro 11 by MacHattie et al. (2014), such that

$$M_{\mathrm{H\,I,abs}} = N_{\mathrm{H\,I,abs}}\, A_{\mathrm{gas}}\, m_{\mathrm{H}}\, f^{3/2}. \qquad (2)$$

The absorbing H I gas column density $N_{\mathrm{H\,I,abs}}$ can be written as a function of spin temperature T_{s} and the optical depth $\tau(v)$ as

$$N_{\mathrm{H\,I,abs}}\,(\mathrm{cm^{-2}}) = 1.823 \times 10^{18}\, T_{\mathrm{s}}\,(\mathrm{K}) \int_{\mathrm{v}} \tau(\mathrm{v})\mathrm{dv}\,(\mathrm{km\,s^{-1}}). \qquad (3)$$

The optical depth can be expressed as a function of the observed change in flux density due to the absorption ΔS, the continuum flux density S_{c}, and the covering fraction of the absorbing gas f as

$$\tau(v) = -\ln(1 + \Delta S(v)/(f\, S_{\mathrm{c}})). \qquad (4)$$

The absorbing gas mass is subject to significant uncertainties, due to the unknown size of the absorbing component, spin temperature, and covering fraction. The radio continuum images (see Fig. 2) indicate that radio emission is produced across the optical body of the galaxy. While the radio continuum is dominated by the contribution of Knot B, the distribution of gas covering the knots is unknown, since neither our observation nor the previous VLA absorption study (MacHattie et al. 2014) resolve the absorption. For this reason, assuming that all of the gas is distributed in front of Knot B would likely lead to a severe underestimation of the H I mass of the absorbing gas. We present the calculation for this hypothesis in Appendix D, but follow a more conservative approach that is informed by the observations at hand in the following. We use the beam size of the VLA observations (7.27 arcsec ×10.07 arcsec) (MacHattie et al. 2014) as an upper limit to the area covered by the absorbing gas. Observations and modelling of the interstellar medium in Haro 11 indicate that the spin temperature is within the range $T_{\mathrm{s}} = 91$–200 K (Cormier et al. 2012; MacHattie et al. 2014). To constrain the covering fraction, we use the values derived from the measurement of the Si_{II} UV absorption line, which is often used as a proxy for studying the neutral gas in galaxies. We use the average covering fraction value of all three knots at deepest absorption velocity v_{min}, yielding $f = 0.82$ (Östlin et al. 2021). Using these parameters, we find an absorbing gas mass $M_{\mathrm{H\,I,abs}} = 3.10 \pm 1.16 \times 10^8\,\mathrm{M_\odot}$.

The total H I mass of Haro 11 is calculated by adding the 21 cm emitting gas mass to the absorbing gas mass, with errors taking into account the uncertainties on both values, dominated by the 21 cm absorbing gas mass uncertainty. This yields a total neutral hydrogen gas mass $M_{\mathrm{H\,I}} = 1.11 \pm 0.20 \times 10^9\,\mathrm{M_\odot}$. This value is higher than previous estimates. Furthermore, the 21 cm image shows the presence of gas with column density well above $N_{\rm H\,I} = 2 \times 10^{20}$ cm^{-2} (see Fig. 1), the empirical efficient self-shielding limit of H I (Kanekar, Braun & Roy 2011). Nevertheless, the H I mass remains smaller than the ionized gas mass (Menacho et al. 2019) 1.8×10^9 M$_\odot$ and the stellar mass (Östlin et al. 2001) of the galaxy $M_* = 1.6^{+2.1}_{-0.6} \times 10^{10}$ M$_\odot$, meaning that neutral gas has been efficiently converted into stars and ionized, likely helping the escape of LyC photons. Most importantly, the neutral gas is strongly offset from LyC production regions, which we discuss hereafter.

5 NEUTRAL GAS GEOMETRY

5.1 Global H I distribution

The H I emission is offset from the main body of the galaxy, in an elongated structure that is ∼ 40 kpc long when projected on the plane of the sky (Fig. 1, panel A). The 21 cm emission components in individual velocity channels are found to be connected spatially and spectrally (especially visible in Fig. B1, but also Fig. B2). Additionally, the [O I]/H α line ratio map, where elevated values trace shocks, shows the largest values ([O I]/H $\alpha > 0.1$) to the north-east of the galaxy (Menacho et al. 2019), towards the direction of the extended neutral gas structure. We have shown the H α and [O I]/H α maps of Haro 11 with H I contours overlaid in Fig. C1. These large values indicate that a shock is occurring at this location. This supports a view with two kinematically distinct gas components, instead of the neutral gas structure being e.g. the result from a continuous outflow from the centre of the galaxy. Together, these observations are consistent with the H I emission structure being a tidal tail from a merger.

The merger nature of Haro 11 had already been demonstrated by ionized gas kinematics studies (Östlin et al. 2001, 2015), but the impact of the interaction on the neutral gas distribution was previously unknown. In fact, the neutral gas structure in Haro 11 strongly resembles a smaller version of the Southern tidal tail in the more massive Antennae galaxy merger (Hibbard et al. 2001), to which Haro 11 has been compared previously due to striking similarity in ionized gas kinematics (Östlin et al. 2015). To further analyse how the merger impacts the neutral gas distribution and star formation in Haro 11 as a function of time, our team has developed simulations of the merger that will be presented in a forthcoming paper (Ejdetjärn et al., in preparation). These simulations use the RAMSES code (Teyssier 2002) and reproduce the H I structure presented here, as well as observations of the stellar populations in the knots (Sirressi et al. 2022). The Haro 11 system was reproduced by the merger of two disc galaxies with respective stellar mass $M_{*,1} = 8 \times 10^9$ M$_\odot$ and $M_{*,2} = 4.6 \times 10^9$ M$_\odot$. The single tidal tail is reproduced in a scenario where the galaxies rotate in opposite ways, with the most massive galaxies having prograde motion, while the least massive one has retrograde motion. According to the simulation, the tail was formed in a period of over 250 Myr after the first close-by interaction between the galaxy nuclei. Haro 11 is currently observed 10–20 Myr after the second close interaction and about 20 Myr before nuclear coalescence. In the simulation, Knots B and C correspond to the nuclei of the initial galaxies, while Knot A is formed in the merging process through tidal motions of the stars.

The asymmetric neutral gas distribution resulting from the merger in Haro 11 likely facilitates the escape of LyC emission in a large fraction of the solid angle, including our own line of sight, and prevents it from other parts. If the tidal tail had been oriented towards the Earth, LyC emission from Haro 11 would most likely not have been detected. The gas with projected column density corresponding to the empirical efficient self-shielding limit of hydrogen 2×10^{20} cm^{-2} (Kanekar, Braun & Roy 2011) (corresponding approximately to the third contour in Fig. 1) covers an angle of 135° from the centre of the galaxy. Making the simplest assumption to estimate the solid angle fraction covered by H I with sufficient column density to efficiently self-shield, which is radial symmetry of the H I gas along the tidal tail axis, we find

$$\Omega_{\rm H\,I} = \int_{\theta_0}^{\theta_f} \sin\theta \, {\rm d}\theta \int_{\phi_0}^{\phi_f} {\rm d}\phi = \int_{0}^{\frac{3\pi}{4}} \sin\theta \, {\rm d}\theta \int_{\frac{\pi}{4}}^{\pi} {\rm d}\phi \simeq 0.32 \, \Omega_{\rm tot}. \tag{5}$$

On large scales characterizing the circumgalactic medium, the merger has thus cleared almost 70 per cent of the solid angle from neutral gas with sizeable column density in Haro 11. Mergers are dynamical phenomena operating on time-scales on the order of hundreds of million years, therefore the position and solid angle covered by neutral gas will change as a function of time. As a result, ionizing radiation escaping from a merger is necessarily strongly anisotropic and varies with time. In the absence of information on the 3D distribution of the gas, the estimation made with present observations is flawed. More precise calculations of the fraction of solid angle covered by neutral gas from each knots, and its evolution as a function of time will be presented in the paper describing simulations of the merger in Haro 11 (Ejdetjärn et al., in preparation).

5.2 H I geometry around LyC-emitting regions

To assess the content and kinematic structure of the neutral gas around the LyC production regions, we extract a spectrum from the non-masked cube at the location of the star-forming knots. This extraction region corresponds to the location of the 21 cm absorbing gas component, since it is unresolved and covers the optical body of Haro 11. The spectrum and extraction aperture are shown in Fig. 3. We find that some 21 cm emission is co-spatial with the star-forming regions and absorption feature, however the channel map in Fig. B2 indicates the components are separated in velocity. We have shown the velocity centroid of the ionized gas emission, which we assume is similar to the velocity of the source emitting the radio continuum emission (consistent with radio emission from star-forming regions). We find that the peak of the 21 cm emission component is redshifted by 92 ± 5 km s^{-1}.

Precisely determining the position of H I gas around the optical body of galaxies is generally difficult. Here, however, we can use reasoning guided by the nature of the radio continuum emission and the velocity distribution of the absorption and emission components to gain some insight on the H I distribution. Analysis of the radio continuum emission indicates the radio continuum is consistent with that of star-forming regions (see Section 3). H I gas that is absorbing radio continuum at 21 cm is necessarily in front of the radio continuum source, which we assume corresponds to star-forming regions in Haro 11. Thus, the blueshift of the absorbing gas compared to the ionized gas centroid indicates that the absorbing gas is outflowing. The maximum velocity of the outflow as compared to the velocity centroid of the H α line is 97 km s^{-1}. Multiphase outflows were already identified around Knots B and A through analysis of the kinematics of emission lines tracing the ionized gas and UV absorption lines from metals tracing a mix of neutral and ionized gas (Sirressi et al. 2022). This study found a maximum velocity of ∼400 km s^{-1}, much larger than the value found with 21 cm absorption. However, metal UV absorption lines do not trace a

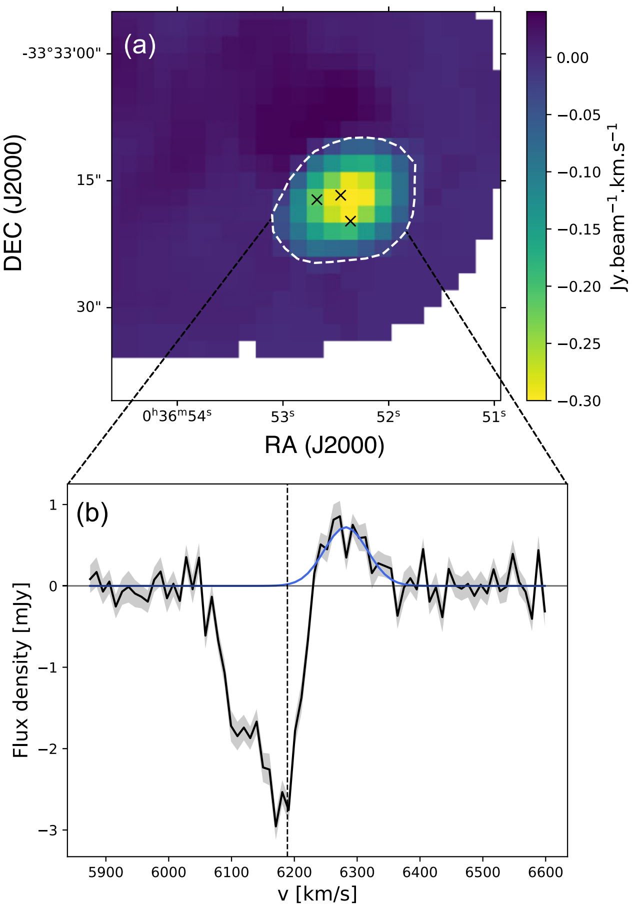

Figure 3. Neutral gas around the LyC production sites. Panel A: MeerKAT high-angular resolution 21 cm integrated flux density map. The dashed white line corresponds to the aperture used to extract the spectrum shown in the lower panel, which traces the limits of the absorption component, determined by collapsing the absorbing gas mask in velocity and applying it as an aperture on the non-masked cube. The crosses indicate the position of the star-forming knots. Panel B: 21 cm spectrum of Haro 11 at the location of the absorption component, shown in black. The blue line shows the Gaussian fit to the emission component seen at this location. The dashed vertical line shows the velocity centroid of the H α line extracted in the same aperture, assumed to indicate the central velocity of the ionized gas around the star-forming regions.

perfectly neutral gas phase, and the excellent agreement between the kinematics from emission lines tracing ionized gas and UV absorption lines in this study could indicate that a significant fraction of the metals are found in the ionized gas phase. Regardless, the blueshift of 21 cm absorption confirms that a neutral gas outflow is occurring in Haro 11.

Having identified that the absorbing gas is outflowing, we then consider the structure of the gas emitting in 21 cm that overlaps with the position of Haro 11. This 21 cm emitting gas is redshifted. While the emitting gas could possibly be located in front of the optical body of the galaxy and inflowing, it is less physically plausible than a scenario where it is behind the star-forming regions. We can reasonably expect the outflow impacting the neutral gas in front of the star-forming regions to impact gas behind the optical body of the galaxy as well. The redshift of the 21 cm-emitting component compared to the centroid of ionized gas is consistent with the picture where this component is outflowing on the back-side of the galaxy, while the absorbing component is outflowing in front of it on our line of sight.

We fit the 21 cm emission component co-spatial with the absorption feature and optical body of the galaxy with a Gaussian using least-squares fitting weighted by errors and integrate the Gaussian profile. We find a flux of 0.062 ± 0.011 Jy km s^{-1} ($1.27 \pm 0.23 \times 10^8$ M$_\odot$), which corresponds to 16 per cent of the total 21 cm *emission* component flux of the galaxy. Most of the H I gas that *emits* in 21 cm is thus found in the tidal tail, away from the star-forming knots. When taking into account the absorbing gas mass which is in front of the galaxy, we find that 25–64 per cent of the total neutral gas mass in the galaxy is offset from the ionizing emission production regions on our line of sight, mostly due to merger-driven interaction. We note that the H I mass seen in emission overlapping with the body of the galaxy (outside of the tidal tail) could be underestimated by our observation, which we discuss in Section 5.4. Nevertheless, the tail contains a significant H I mass of $6.72 \pm 0.88 \times 10^8$ M$_\odot$. In the following, we compare the H I offset in Haro 11 to typical values from normal star-forming galaxies.

5.3 H I offset calculation

We observe an offset of the 21 cm emitting gas from the centre of the galaxy. In order to estimate if this offset is significant, we calculate the centroid coordinates x_c, y_c of the 21 cm emission and 21 cm absorption separately, using the following expression, where x_i and y_i are the pixel coordinates on the x and y axes and I_i the pixel value at x_i, y_i:

$$x_c = \frac{\sum_i x_i \times I_i}{\sum_i I_i} \ , \ y_c = \frac{\sum_i y_i \times I_i}{\sum_i I_i}. \tag{6}$$

The centroid of 21 cm mass in Haro 11 is then calculated by taking the average of the 21 cm emission and absorption centroid coordinates, weighted by the mass fraction in each component, and taking into account the uncertainties on both mass values.

We investigate how this neutral gas offset compares with galaxies of similar stellar mass in the THINGS sample of nearby galaxies (de Blok et al. 2008; Walter et al. 2008). Specifically, we select galaxies with stellar masses 10^{10} M$_\odot$ $< M_* <$ 10^{11} M$_\odot$ in de Blok et al. (2008), and calculate the 21 cm emission centroid in the publicly available moment-0 maps with robust weighting using equation (6). We derive the 21 cm emission centroid of NGC 925, NGC 2903, NGC 3198, NGC 3621, NGC 4736, and NGC 6946,[1] and compare it to that of Haro 11, accounting for the large uncertainty on the absorbing gas mass (see Table 4).

We find an average offset of 0.82 kpc for the THINGS galaxies, with all galaxies having 21 cm emission centroids within 2 kpc of the optical coordinates. In contrast, the 21 cm centroid in Haro 11 is offset by $6.28^{+3.64}_{-3.41}$ kpc, 4–12 times larger than the average centroid offset for THINGS galaxies. We have also quantified the offset to individual knots: the centroid of the gas is offset by $8.89^{+3.64}_{-3.41}$, $7.71^{+3.64}_{-3.41}$, and $6.46^{+3.64}_{-3.41}$ kpc, respectively, from Knots A, B, and C. We have shown the relative offset of the 21 cm centroid compared to the central galaxy coordinates in physical units in Fig. 4. The 21 cm centroids are shown overlaid on 21 cm emission moment-0 maps for each galaxy in Fig. E1. In general, neutral gas does not perfectly overlap with stellar regions in galaxies. However, the neutral gas in Haro

---

[1] NGC 3031 is also in the stellar mass range considered, but imaging artefacts (Walter et al. 2008) prevent an accurate calculation of the 21 cm emission centroid.

Table 4. Distance offset of the 21 cm emission centroid to the optical coordinates of the galaxy. The uncertainties on the centroid offset in Haro 11 are due to the uncertainties of the absorbing gas mass located in front of the galaxy.

ID	21 cm centroid offset (kpc)
Haro 11	$6.28^{+3.64}_{-3.41}$
Haro 11, em	16.51
Haro 11, abs	2.04
NGC 925	1.30
NGC 2903	0.32
NGC 3198	0.31
NGC 3621	0.37
NGC 4736	0.67
NGC 6946	1.96

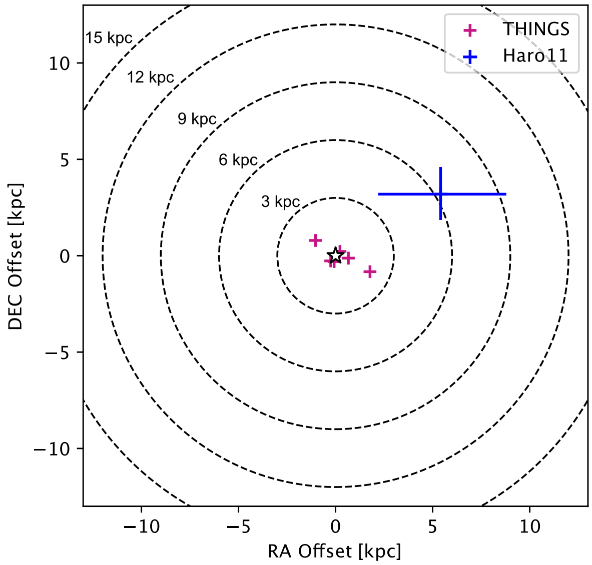

Figure 4. Relative 21 cm centroid offset compared to the galaxy optical coordinates. The centre of the galaxies is shown by the star in the centre. The position of the 21 cm emission centroid is shown by purple crosses for galaxies in the THINGS sample (Walter et al. 2008) with stellar masses in the range [10^{10}–10^{11} $M_{\odot}$]. The position of the Haro 11 H I centroid is indicated by the blue cross, with error bars taking into account the uncertainty on the 21 cm absorption component contribution to the H I mass. Dashed lines indicate offsets from the centre in multiples of 3 kpc.

11 has undergone a bulk offset from the centre of the galaxy, where the LyC-emitting regions are located. This global offset caused by a merger interaction is likely facilitating the escape of LyC photons from the centre of the galaxy into our line of sight.

5.4 Caveats

While the MeerKAT observation improves upon previous work on the neutral gas mass and distribution of Haro 11, we note that the 21 cm absorption remains unresolved. Similarly to the way in which the emission and absorption cancelled each other out in the GBT observation, causing the absorption feature to be missed by previous single-dish study, the MeerKAT observation could be missing part of the mass around the centre of the galaxy due to angular resolution limits. In order to improve upon the H I mass measurement obtained here, observations with both excellent sensitivity and resolution close to the angular size of the knots (∼2 arcsec) will be required. Observing a deeper absorption feature at lower angular resolution would likely not affect the H I mass in absorption significantly due to the decrease in mass when considering smaller gas-covering areas (see equation 2 and Appendix D). However, this could cause an increase of the H I mass in the neutral gas component seen in emission that is overlapping with the optical body of the galaxy. Nevertheless, the offset of a large amount of H I gas from our line of sight certainly facilitates the escape of LyC photons in our direction. If this mass was instead distributed uniformly within the area of the beam, the additional column density along the line of sight would be 1.8×10^{21} cm^{-2}. If the mass in the tail was distributed in a larger area corresponding twice the beam size, as one could reasonably expect given neutral gas usually extends beyond the optical body of normal galaxies, the corresponding column density would be 4.5×10^{20} cm^{-2}. Even when assuming that the LyC photons would ‘see’ only half of this column density, these values are optically thick to LyC radiation by several orders of magnitude. Therefore, the tidal displacement of the gas outside of our line of sight effectively lowers the column density seen by LyC photons, and facilitates the ionizing radiation escape into the intergalactic medium.

6 DISCUSSION

The H I morphology and kinematics of Haro 11 demonstrate that large-scale pathways devoid of neutral gas with significant column density exist around this galaxy, likely facilitating LyC escape from the circumgalactic medium on several lines of sight. These observations provide a potential link between dwarf galaxy mergers and the detection of LyC emission from galaxies. Galaxy mergers in low-mass systems could play several roles in facilitating the escape of LyC emission from galaxies. First, mergers create multiple star formation bursts (Lahén et al. 2020) during the time-scale of the interaction by repeatedly compressing the gas at the centre of the galaxy. These bursts create numerous massive stars, which produce the bulk of LyC emission in galaxies; thus, mergers increase the intrinsic LyC photon production. Secondly, starbursts are also responsible for the intense feedback that creates ionized channels enabling the escape of LyC photons from their immediate environment (Clarke & Oey 2002; Borthakur et al. 2014). Finally, since merger interactions lead to the efficient conversion of gas into stars in the central parts of galaxies, and the ionization of remaining H I or displacement of it in tidal structures away from the star-forming regions (Georgakakis, Forbes & Norris 2000), they effectively lead to a bulk offset of the material inhibiting LyC escape from the centre of interacting galaxies. This effect, imaged here in a galaxy that is close to nuclear coalescence, is likely to strongly depend on the time-scale of the merger interaction and the viewing angle of the merging system, with a fraction of the lines of sight being obscured by tidal structures. However, by creating regions depleted of H I on large scales, galaxy mergers are interesting mechanisms that can facilitate the anisotropic escape of LyC photons out of the interstellar medium and into the intergalactic medium. Other environmental effects, such as ram pressure stripping of neutral gas in high-density environments, produce similar effects on the neutral gas of galaxies. These processes can also promote star formation on the edges of stripped tails, which could lead to LyC escape (e.g. Kenney et al. 2014). However, there has been no observation of LyC emission from galaxies undergoing such environmental effect so far.

In the local Universe, two other LyC-emitting galaxies have been detected that are close enough to be imaged with interferometers: Tol 1247–232 and Mrk 54 (Leitherer et al. 2016). Both of these galaxies show prominent merger morphologies in the optical, however their neutral gas content is significantly different, with Mrk 54 having a high HI mass $M_{\mathrm{H\,I}} = 1.6 \pm 0.2 \times 10^{10}\,\mathrm{M}_{\odot}$ (Haynes et al. 2018), while Tol 1247–232 has not yet been detected in 21 cm, and has currently only an upper limit on the mass $M_{\mathrm{H\,I}} < 1 \times 10^{9}\,\mathrm{M}_{\odot}$ (Puschnig et al. 2017). Given the morphology of these galaxies in the optical, it is likely that a fraction of their HI gas has been removed by tidal interactions from the lines of sight where LyC is emitted. This would facilitate the ionization by the starburst and explain how LyC emission can escape from environments with such different neutral gas properties.

While they are not directly detected, many galaxies are considered to be LyC candidates due to their peculiar Ly α line profile shapes or their high [O III]/[O II] ratios, which indirectly trace LyC escape (Verhamme et al. 2015; Izotov et al. 2018; Flury et al. 2022a, b). Among these candidates, many display signs of ongoing merger events. Green pea galaxies are a class of objects considered excellent analogues of high-redshift LyC-emitting galaxies (Cardamone et al. 2009; Izotov et al. 2016). Single-dish 21 cm line measurements of green pea galaxies have suggested that galaxies with high [O III]/[O II] ratios are less likely to be detected in 21 cm, potentially indicating that galaxies with low H I mass are more likely to leak LyC radiation (Kanekar et al. 2021). However, about a fifth of the sample of green pea galaxies studied in 21 cm have neutral gas and galaxy properties indicative of either recent gas accretion or the presence of a gas-rich companion. Recently, H I imaging of the green pea galaxy J0213+0056 has shown that a merger could explain Ly α escape in the galaxy, and could potentially lead to LyC leaking (Purkayastha et al. 2022). One study of the environment of a small sample of green pea galaxies using optical emission lines has found that these galaxies do not have a higher companion fraction than less star-forming line-and continuum-selected galaxies at comparable stellar mass (Laufman et al. 2022). However, this result does not exclude these objects being the product of mergers close to nuclear coalescence, which could be investigated by studies of low surface brightness tidal features in these galaxies.

The galaxy merger rate is difficult to measure in the early Universe; however, a few observational studies have found indications of an increase in merger rate at redshift 4 and up to 6 (Tasca et al. 2014; Duncan et al. 2019). From the simulation perspective, galaxy mergers also seem to be a promising process facilitating the escape of ionizing LyC radiation during the Epoch of Reionization. Indeed, cosmological hydrodynamical simulations predict an increase of mergers with increasing redshift (Rodriguez-Gomez et al. 2015). Semi-analytical galaxy formation models also show that galaxies found in dense environments reside in larger ionized regions (Qin et al. 2022), with galaxies having neighbors being more likely to show Ly α emission at $z = 8$. However, the environment of galaxies leaking LyC emission has not yet been studied in a systematic way, leaving uncertainties on their possible contribution to Reionization.

7 CONCLUSION

We have observed the neutral gas reservoir of the LyC-emitting galaxy Haro 11 with the 21 cm H I line. We detect a previously known unresolved 21 cm absorption component overlapping with the galaxy, and resolve the 21 cm emission, hereby providing the first map of the material preventing ionizing radiation escape in a LyC emitter. By calculating the mass in the 21 cm absorbing and emitting components separately, we find a neutral gas mass $M_{\mathrm{H\,I}} = 1.11 \pm 0.20 \times 10^{9}\,\mathrm{M}_{\odot}$, larger than previous estimates from unresolved measurements in which these components averaged each other. We also find that the neutral gas is distributed in a ~ 40 kpc-long tidal tail resulting from a merger interaction. This gas tail connects with the optical body of the galaxy, around which the neutral gas is outflowing. We find that 44^{+20}_{-19} per cent of the neutral gas mass resides in the tidal tail, and the gas has undergone a bulk offset of $6.28^{+3.64}_{-3.41}$ kpc from the centre of the galaxy, about seven times larger than the mean offset between optical coordinates and 21 cm emission for galaxies of similar mass in the THINGS survey. Additionally, we estimate that on large scale, the merger interaction has cleared about 70 per cent of the solid angle from dense gas with the ability to self-shield against ionizing radiation ($N_{\mathrm{H\,I}} > 2 \times 10^{20}\,\mathrm{cm}^{-2}$) by displacing a large fraction of the gas into the tidal tail and ionizing remaining gas surrounding the centre.

The merger interaction is likely the mechanism that allows us to observe ionizing radiation from Haro 11, since it has increased the star formation rate in the centre of the galaxy, leading to increased LyC production and to the creation of ionized channels, and has offset a large fraction of the material which inhibits LyC escape from star-forming regions from our line of sight. While mergers are likely not the only mechanism responsible for LyC escape from galaxies, they are an effective process that unites several of the conditions required for ionizing photons to escape to the intergalactic medium. Their contribution to reionization has not yet been evaluated in detail. The impact of galaxy environment on LyC escape should be assessed from the point of view of simulations and observations alike.

ACKNOWLEDGEMENTS

ALR thanks Christian Binggeli, Alba Covelo Paz, and Mohammad Javad Shahhoseini for their contributions to the pilot 21 cm interferometric observing proposal for Haro 11. JMC and JLI were supported by NSF/AST-2009894. JMC and SHT acknowledge support from Macalester College. MJH is fellow of the Knut & Alice Wallenberg Foundation. AA acknowledges financial support from the Swedish Research Council (VR) under grant 2021-05559. GÖ acknowledges financial support from the Swedish Research Council (VR) and the Swedish National Space Agency (SNSA). The MeerKAT telescope is operated by the South African Radio Astronomy Observatory, which is a facility of the National Research Foundation, an agency of the Department of Science and Innovation. The National Radio Astronomy Observatory is a facility of the National Science Foundation operated under cooperative agreement by Associated Universities Inc. This study uses observations made with ESO Telescopes at the La Silla Paranal Observatory under programme IDs 094.B-0944(A) and 096.B-0923(A). This work made use of THINGS, 'The HI Nearby Galaxy Survey' (Walter et al. 2008).

DATA AVAILABILITY

The data sets generated and analysed in this study will be made publicly available in the SARAO DataCite repository.

REFERENCES

Adamo A., Zackrisson E., Östlin G., Hayes M., 2010, ApJ, 725, 1620
Barkana R., 2006, Science, 313, 931
Berg D. A., Chisholm J., Erb D. K., Pogge R., Henry A., Olivier G. M., 2019, ApJ, 878, L3
Bergvall N., Masegosa J., Östlin G., Cernicharo J., 2000, A&A, 359, 41
Bergvall N., Zackrisson E., Andersson B. G., Arnberg D., Masegosa J., Östlin G., 2006, A&A, 448, 513
Borthakur S., Heckman T. M., Leitherer C., Overzier R. A., 2014, Science, 346, 216

CASA Team, 2022, PASP, 134, 114501
Cardamone C. et al., 2009, MNRAS, 399, 1191
Clarke C., Oey M. S., 2002, MNRAS, 337, 1299
Cormier D. et al., 2012, A&A, 548, A20
Dayal P. et al., 2020, MNRAS, 495, 3065
Duncan K. et al., 2019, ApJ, 876, 110
Flury S. R. et al., 2022a, ApJS, 260, 1
Flury S. R. et al., 2022b, ApJ, 930, 126
Gao Y. et al., 2022, A&A, 661, A136
Gazagnes S., Chisholm J., Schaerer D., Verhamme A., Rigby J. R., Bayliss M., 2018, A&A, 616, A29
Georgakakis A., Forbes D. A., Norris R. P., 2000, MNRAS, 318, 124
Ghara R., Choudhury T. R., Datta K. K., Choudhuri S., 2017, MNRAS, 464, 2234
Gross A. C., Prestwich A., Kaaret P., 2021, MNRAS, 505, 610
Haynes M. P. et al., 2018, ApJ, 861, 49
Hibbard J. E., van der Hulst J. M., Barnes J. E., Rich R. M., 2001, AJ, 122, 2969
Izotov Y. I., Orlitová I., Schaerer D., Thuan T. X., Verhamme A., Guseva N. G., Worseck G., 2016, Nature, 529, 178
Izotov Y. I., Worseck G., Schaerer D., Guseva N. G., Thuan T. X., Fricke Verhamme A., Orlitová I., 2018, MNRAS, 478, 4851
Kanekar N., Braun R., Roy N., 2011, ApJ, 737, L33
Kanekar N., Ghosh T., Rhoads J., Malhotra S., Harish S., Chengalur J. N., Jones K. M., 2021, ApJ, 913, L15
Kenney J. D. P., Geha M., Jáchym P., Crowl H. H., Dague W., Chung A., van Gorkom J., Vollmer B., 2014, ApJ, 780, 119
Kepley A. A., Tsutsumi T., Brogan C. L., Indebetouw R., Yoon I., Mason B., Donovan Meyer J., 2020, PASP, 132, 024505
Klein U., Lisenfeld U., Verley S., 2018, A&A, 611, A55
Kulkarni G., Worseck G., Hennawi J. F., 2019, MNRAS, 488, 1035
Kunth D., Leitherer C., Mas-Hesse J. M., Östlin G., Petrosian A., 2003, ApJ, 597, 263
Lahén N., Naab T., Johansson P. H., Elmegreen B., Hu C.-Y., Walch S., Steinwandel U. P., Moster B. P., 2020, ApJ, 891, 2
Laufman L., Scarlata C., Hayes M., Skillman E., 2022, ApJ, 940, 31
Leitet E., Bergvall N., Hayes M., Linné S., Zackrisson E., 2013, A&A, 553, A106
Leitherer C., Hernandez S., Lee J. C., Oey M. S., 2016, ApJ, 823, 64
MacHattie J. A., Irwin J. A., Madden S. C., Cormier D., Rémy-Ruyer A., 2014, MNRAS, 438, L66
Menacho V. et al., 2019, MNRAS, 487, 3183
Östlin G., Amram P., Bergvall N., Masegosa J., Boulesteix J., Márquez I., 2001, A&A, 374, 800
Östlin G., Hayes M., Kunth D., Mas-Hesse J. M., Leitherer C., Petrosian A., Atek H., 2009, AJ, 138, 923
Östlin G., Marquart T., Cumming R. J., Fathi K., Bergvall N., Adamo A., Amram P., Hayes M., 2015, A&A, 583, A55
Östlin G. et al., 2021, ApJ, 912, 155
Pardy S. A., Cannon J. M., Östlin G., Hayes M., Bergvall N., 2016, AJ, 152, 178
Planck Collaboration VI, 2020, A&A, 641, A6
Prestwich A. H., Jackson F., Kaaret P., Brorby M., Roberts T. P., Saar S. H., Yukita M., 2015, ApJ, 812, 166
Purkayastha S., Kanekar N., Chengalur J. N., Malhotra S., Rhoads J., Ghosh T., 2022, ApJ, 933, L11
Puschnig J. et al., 2017, MNRAS, 469, 3252
Qin Y., Wyithe J. S. B., Oesch P. A., Illingworth G. D., Leonova E., Mutch S. J., Naidu R. P., 2022, MNRAS, 510, 3858
Rau U., Cornwell T. J., 2011, A&A, 532, A71
Roberts M. S., 1962, AJ, 67, 437
Robertson B. E., Ellis R. S., Dunlop J. S., McLure R. J., Stark D. P., 2010, Nature, 468, 49
Rodriguez-Gomez V. et al., 2015, MNRAS, 449, 49
Saldana-Lopez A. et al., 2022, A&A, 663, A59
Schmitt H. R., Calzetti D., Armus L., Giavalisco M., Heckman T. M., Kennicutt R. C. J., Leitherer C., Meurer G. R., 2006, ApJS, 164, 52
Senchyna P. et al., 2017, MNRAS, 472, 2608
Serra P. et al., 2015, MNRAS, 448, 1922
Sirressi M. et al., 2022, MNRAS, 510, 4819
Taft S., Cannon J. M., Pardy S., Hayes M., Östlin G., Bergvall N., Rivera-Thorsen T., Puschnig J., 2019, in American Astronomical Society Meeting Abstracts #233. p. 368.10
Tasca L. A. M. et al., 2014, A&A, 565, A10
Teyssier R., 2002, A&A, 385, 337
Trebitsch M., Hutter A., Dayal P., Gottlöber S., Legrand L., Yepes G., 2023, MNRAS, 518, 3576
Verhamme A., Orlitová I., Schaerer D., Hayes M., 2015, A&A, 578, A7
Walter F., Brinks E., de Blok W. J. G., Bigiel F., Kennicutt Robert C. J., Thornley M. D., Leroy A., 2008, AJ, 136, 2563
de Blok W. J. G., Walter F., Brinks E., Trachternach C., Oh S. H., Kennicutt R. C. J., 2008, AJ, 136, 2648

APPENDIX A: OPTICAL AND RADIO CONTINUUM EMISSION COMPARISON

In Fig. A1, we present a comparison of radio continuum and stellar emission. Radio continuum emission contours and the 21 cm absorption centroid are overlaid on an *HST F435W* filter image of the stellar emission in Haro 11. Colourful contours highlight the location of the unresolved continuum source in Knot B, while white contour trace the morphology of the radio continuum emission with the highest resolution radio continuum image.

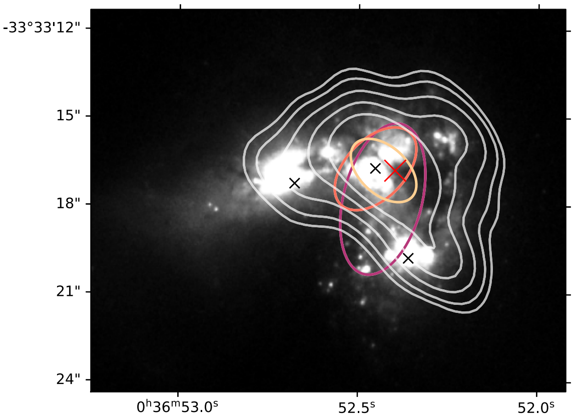

Figure A1. Radio continuum and optical stellar emission comparison. *HST F435W* filter image with VLA continuum emission contours overlaid in pink for the *S*-band (3 GHz), in orange for the *X*-band (9.8 GHz), in yellow and white for the *Ka*-band (33 GHz). The contours for each band are also presented in Fig. 2. The colourful contours correspond to the Gaussian aperture used to extract the flux in Knot B, while the white contours show the *Ka*-band continuum at the $\{3, 5, 10, 20, 40\} \times \sigma$ levels. Black crosses indicate the position of the three star-forming knots, the red cross indicates the position of the 21 cm absorption centroid.

APPENDIX B: 21 CM MORPHO-KINEMATICS

Channel maps of the 21 cm of Haro 11 are shown for the high-resolution and intermediate-resolution cubes in Figs B2 and B1. A large fraction of the 21 cm emission is found in an extended feature that is connected both spatially and spectrally and is offset from the centre of the galaxy. This morphology, along with previous observations concluding to the merger nature of Haro 11 (Östlin et al. 2015), and the reproduction of the neutral gas structure with simulations, strongly suggest that the extended 21 cm emission traces a tidal tail resulting from the merger interaction.

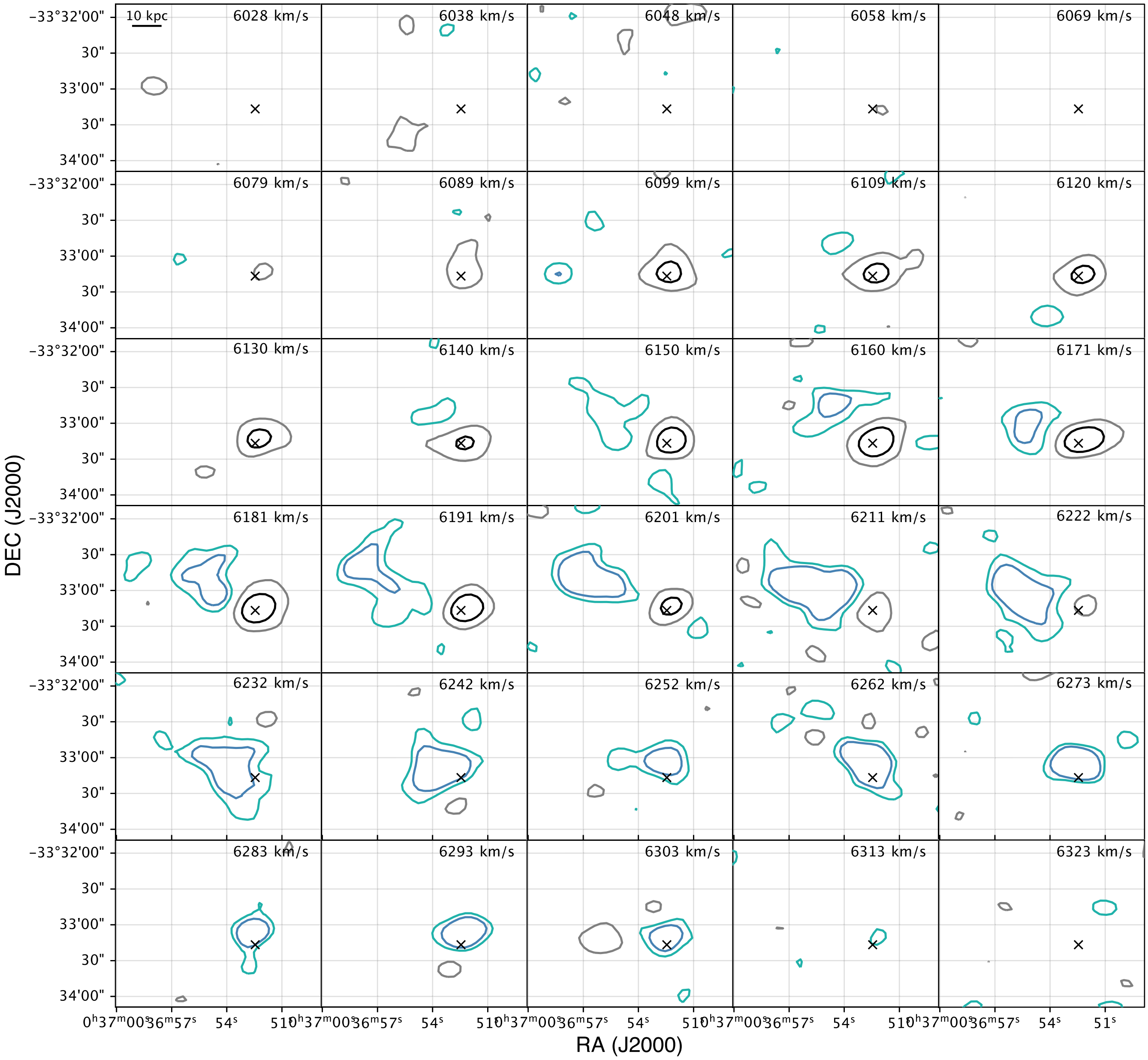

Figure B1. MeerKAT intermediate angular resolution 21 cm channel map. Levels displayed correspond to the -10σ, -3σ, 3σ, and 5σ levels, respectively, shown in black, grey, light blue, and dark blue. The position of Knot B is indicated by a cross. The two other knots are extremely close to Knot B, they have not been represented here to help readability.

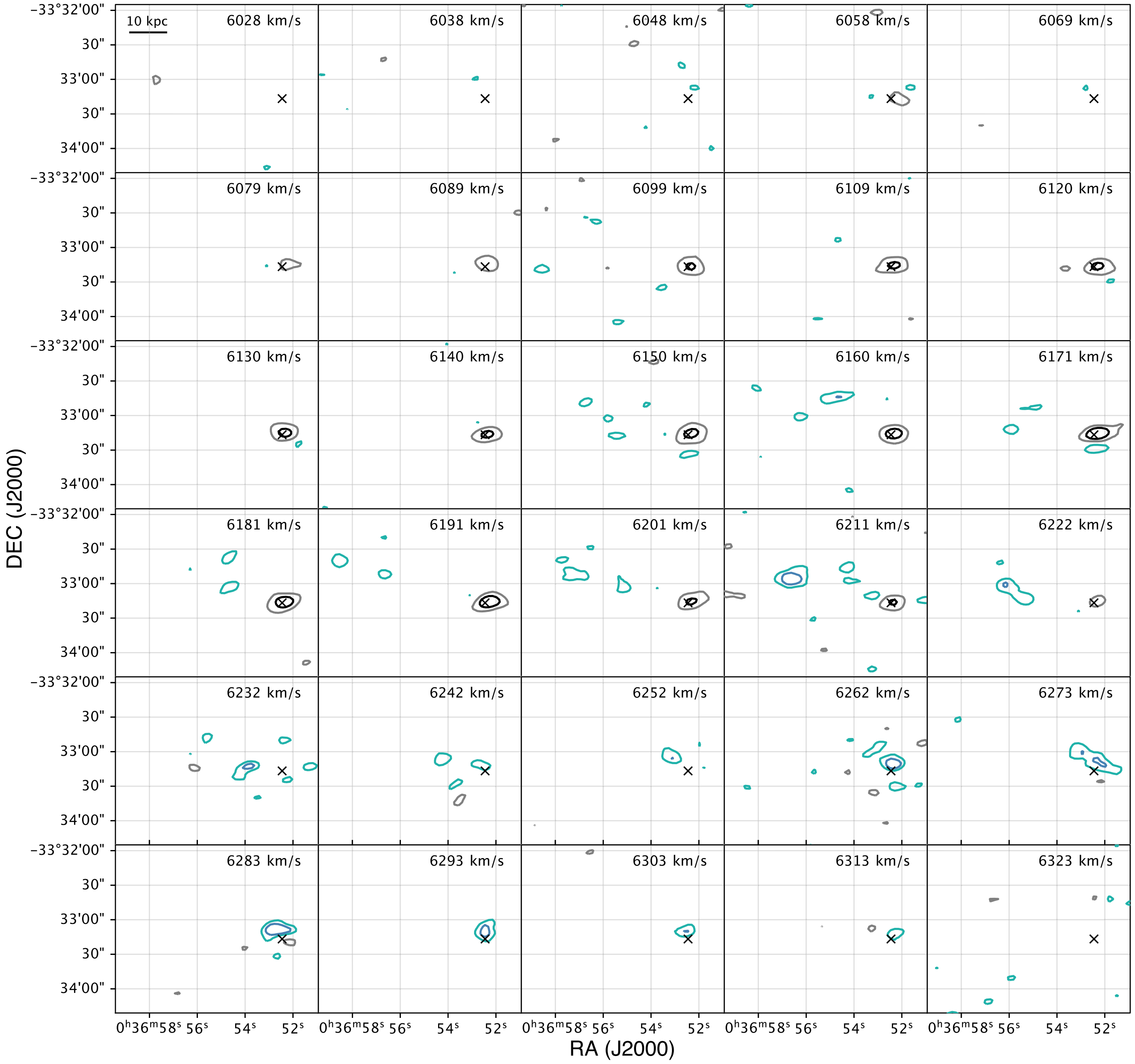

Figure B2. MeerKAT high-angular resolution 21 cm channel map. Levels displayed correspond to the -10σ, -3σ, 3σ, and 5σ levels, respectively, shown in black, grey, light blue, and dark blue. The position of Knot B is indicated by a cross. The two other knots are extremely close to Knot B, they have not been represented here to help readability.

APPENDIX C: IONIZED GAS MAPS

Ionized gas maps from MUSE with neutral gas contours are presented in Fig. C1. The ionized gas is distributed in a large halo surrounding the knots as seen in the Hα line map on the top panel. The [O I]/Hα line ratio map, shown on the bottom panel, traces shocks, which can be identified by elevated value of the ratio. Interestingly, elevated values of the ratio ([O I]/H$\alpha > 0.1$) tracing a highly shocked feature are seen on the north-eastern part of the Haro 11, towards high H I column density regions. This occurs in regions where the extended neutral gas structure reconnects with the optical body of the galaxy. The most promising explanation for this feature is one where the cold dense gas provides a working surface to shock hot, outflowing material. This can be explained by the existence of an outflow around the optical body of the galaxy, that is shocking the gas found in the neutral tidal tail.

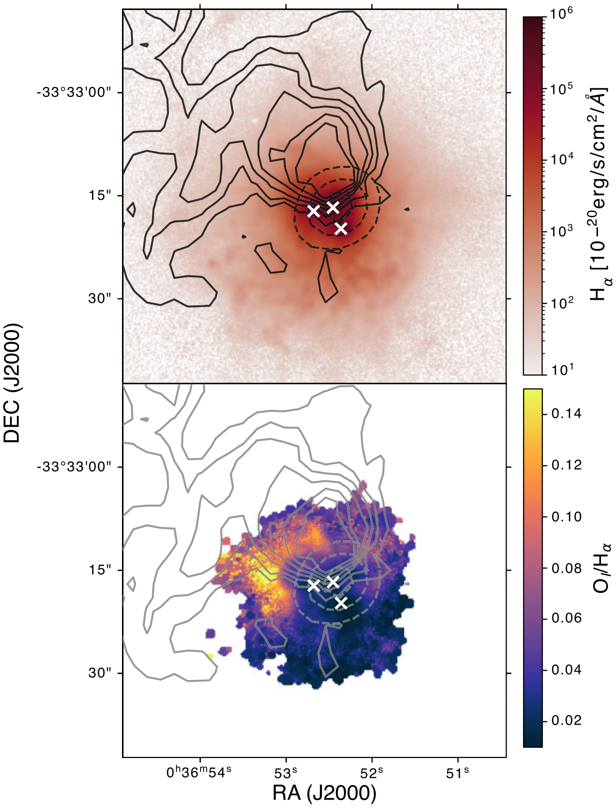

Figure C1. MUSE ionized gas maps with H I contours overlaid. The top panel shows the H α moment-0 map, while the bottom panel shows the [O I]/H α ratio map. The H I contours shown in black and grey in the two panels are the same as in Fig. 1. The white crosses indicate the positions of the star-forming knots. North is up and East is to the left.

APPENDIX D: A CASE WHERE THE ABSORBING NEUTRAL GAS MASS IS CONCENTRATED IN FRONT OF KNOT B

Here we consider a case where the neutral gas seen in absorption would be concentrated in front of the radio continuum source overlapping with Knot B. We follow the same method outlined in Section 4, but adjust the parameters used to calculate the mass. We use the gas covering fraction $f = 0.96$ derived for Knot B (Östlin et al. 2021) and use the upper limit to the size of the radio continuum source derived with *Ka*-band imaging (1.66 arcsec × 2.71 arcsec). We approximate the continuum flux in Knot B at 1.4 GHz as 25 mJy by extrapolating the radio continuum SED fit. These parameters yield an absorbing gas mass $M_{\text{H I,abs}} = 2.8 \pm 1.1 \times 10^7\,\text{M}_\odot$. However, due to angular resolution limits of our observation, we cannot determine if the absorbing gas is in fact fully distributed in front of this knot. UV absorption line observations of the knots identify neutral gas outflows in front of other parts of the galaxy, indicating that Knot B is not the only region covered by neutral gas in the galaxy (Sirressi et al. 2022). Nevertheless, we note that if the hypothesis of neutral gas fully covering Knot B held true, and no additional gas was observed in emission around the other knots, it would increase both the fraction of mass seen in emission ($93.2^{+2.9}_{-3.5}$ per cent), and the associated neutral gas centroid offset (∼ 15 kpc).

APPENDIX E: 21 CM EMISSION CENTROID IN HARO 11 AND THINGS GALAXIES

We show the position of 21 cm centroids of Haro 11 and THINGS galaxies of similar stellar mass in Fig. E1. The centroids, shown by purple or blue crosses, are overlaid on 21 cm emission images, and are compared to the optical coordinates indicated by white stars. For Haro 11, we have also overlaid the 21 cm absorption contours, which are taken into account when calculating the 21cm centroid.

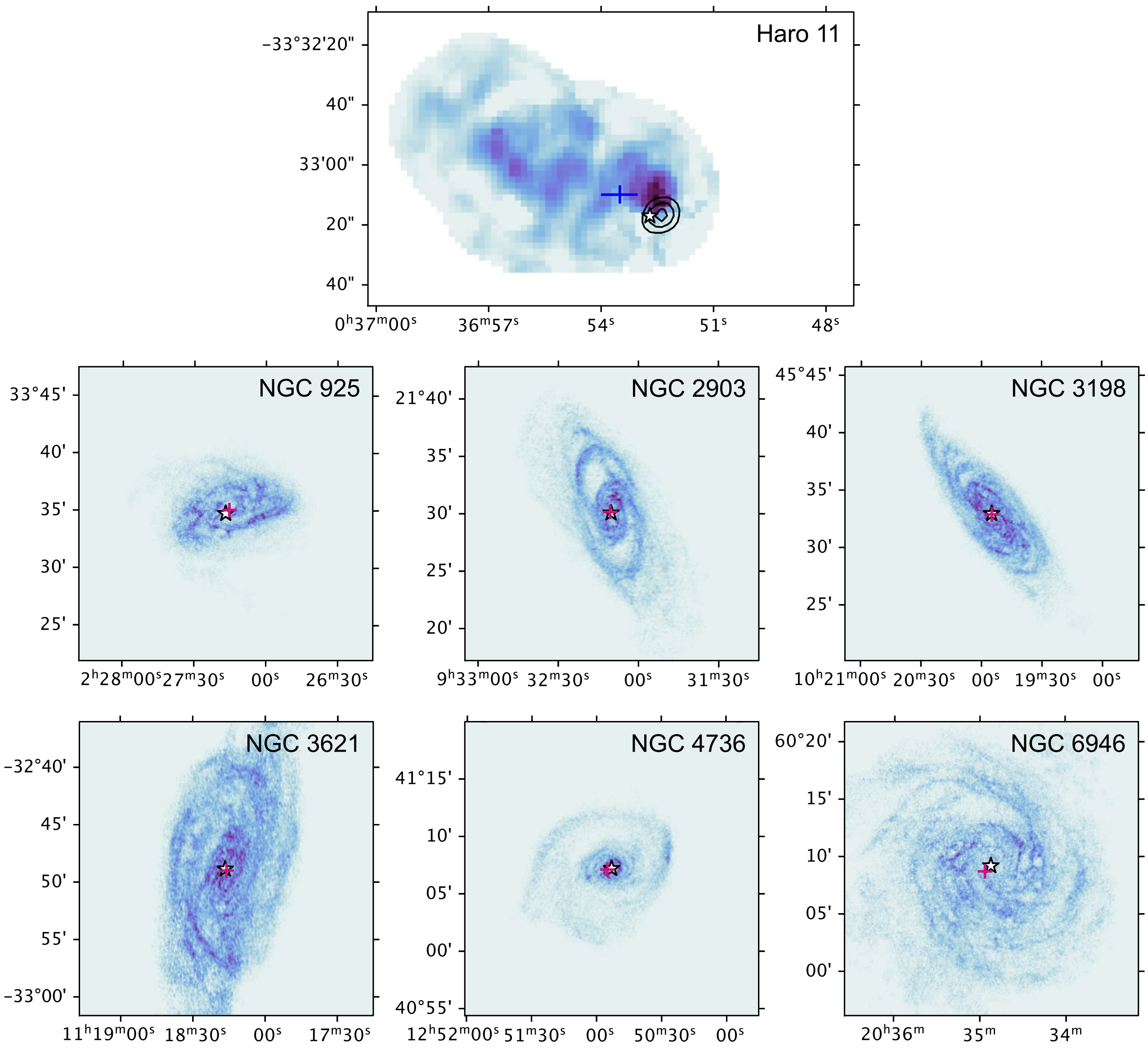

Figure E1. Position of 21 cm centroids compared to the optical coordinates in Haro 11 and THINGS galaxies of similar stellar mass, overlaid on 21 cm emission images. In each image, the optical coordinates of the galaxies are indicated by a star. The 21 cm centroid of Haro 11 (top panel) is indicated by a blue cross with error bars taking into account the uncertainty in absorbing gas mass. We show the same contours of 21cm absorbing gas as in Fig. 1. The 21 cm emission centroids of THINGS galaxies are shown by purple crosses.

This paper has been typeset from a TEX/LATEX file prepared by the author.